



TiO₂ photocatalyst for indoor air remediation: Influence of crystallinity, crystal phase, and UV radiation intensity on trichloroethylene degradation

Valeria Puddu ^{a,1}, Hyeok Choi ^b, Dionysios D. Dionysiou ^c, Gianluca Li Puma ^{a,*}

^a Photocatalysis and Photoreaction Engineering, Department of Chemical and Environmental Engineering, University of Nottingham, Nottingham, NG7 2RD, UK

^b Department of Civil Engineering, University of Texas at Arlington, 416 Yates Drive, Arlington, TX 76019-0308, USA

^c Department of Civil and Environmental Engineering, University of Cincinnati, Cincinnati, OH 45221-0071, USA

ARTICLE INFO

Article history:

Received 8 May 2009

Received in revised form 28 July 2009

Accepted 3 August 2009

Available online 8 August 2009

Keywords:

Indoor air treatment

Titanium dioxide

Photocatalysis

Trichloroethylene

Degussa P-25

Crystal phase

Anatase

Rutile

UV radiation intensity

ABSTRACT

Nanocrystalline TiO₂ photocatalysts prepared through a simple sol–gel process followed by calcination at 100–800 °C were evaluated for the decomposition of trichloroethylene (TCE) in simulated indoor air. Catalysts made of pure anatase, anatase/rutile mixture and pure rutile with crystal sizes of 5.8–75.8 nm and surface areas of 4.3–498 m²/g were immobilized as thick films on borosilicate glass and installed in a gas-phase, flat-plate photocatalytic reactor. Pure anatase TiO₂ treated at 300–600 °C exhibited higher activity than commercial TiO₂ (P-25) under UV-A radiation with intensity of 5.1, 14.0 and 20.8 W/m². Conversely, pure rutile and mixed phase TiO₂ materials showed significantly lower activity. The photocatalytic activity of fully grown anatase TiO₂ with crystal size of 27 nm was up to three-fold higher than that of P-25 despite exhibiting lower surface area. The increase in the crystallinity of anatase TiO₂ upon calcination overcame the depreciation in its structural properties (decrease in surface area and porosity) for the decomposition of TCE. The dependence of the TCE oxidation rate on the intensity of the incident radiation in the range 5.2–20.8 W/m² was found to be first-order for the samples containing a rutile phase (including P-25) and 0.75-order for the sample containing pure anatase suggesting that “absorbed” photons are more effectively used when a rutile phase is present. However, less number of incident photons are absorbed by samples with pure rutile compared to samples with pure anatase. The crystallographic properties of TiO₂ over its structural properties were found to be essential factors which determined the higher photocatalytic activity of TiO₂ anatase for the photocatalytic decomposition of TCE. Rate equations for the photocatalytic oxidation of TCE over TiO₂ films derived from an elementary reaction mechanism and with explicit effect of the incident photon flux were correlated with the catalyst properties.

© 2009 Elsevier B.V. All rights reserved.

1. Introduction

Indoor air pollutants are different in type and concentration from outdoor pollutants. Indoor air pollution is due mainly to volatile organic compounds (VOCs) that are widely emitted by common household products and building materials such as furniture, paints, varnish, sealants, flame retardants and cleaning goods. VOCs are released as vapors in the indoor environment at ambient temperature and pressure. Long-term exposure, even to relatively low concentration of VOCs may have several adverse

effects on human health. Poor indoor air is also the main cause of “sick building syndrome” and consequent decrease in human productivity. For these reasons, indoor air quality is a matter which is gaining significant attention by environmental protection agencies worldwide. Recent studies have concluded that efficient and economical remediation processes are required in both public buildings and private houses.

Photocatalytic oxidation (PCO) using semiconductors as photocatalysts, represent an excellent technology for environmental remediation. In particular, PCO based on TiO₂ has been demonstrated to be highly effective in the treatment of contaminated water and air [1–5]. PCO appears to be a highly promising technology for application in indoor air purification. TiO₂ is an inexpensive, stable, non toxic semiconductor with a large band gap (3.2 eV for anatase and 3.0 eV for rutile) and with a strong oxidizing power. Photooxidation on TiO₂ surface irradiated with suitable UV radiation ideally leads to complete mineralization of

* Corresponding author. Tel.: +44 (0) 115 9514170; fax: +44 (0) 115 9514115.
E-mail address: gianluca.li.puma@nottingham.ac.uk (G. Li Puma).

¹ Present address: Biomolecular and Materials Interface Research Group, School of Science and Technology, Nottingham Trent University, Clifton Lane, Nottingham, NG11 8NS, UK.

VOCs to environmentally friendly species such as water, carbon dioxide and mineral acids. TiO_2 exists in three different crystalline forms: anatase, rutile and brookite. Anatase and rutile are the most studied polymorphs for photocatalytic applications. Even if the photocatalytic activity is highly specific and depends on the target contaminant under study (i.e. dyes, organic acids, amines, alcohols, chlorohydrocarbons) [6], anatase is usually recognized as the most active form of titania. P-25 (Degussa) TiO_2 catalyst, a 1:4 mixture of rutile and anatase, has been, and continues to be, the preferred choice in many studies due to its high activity and commercial availability. P-25 has been considered as a reference in the evaluation of the activity of TiO_2 materials developed.

Trichloroethylene (TCE), a solvent, cleaning and a degreasing agent, is a common VOC in indoor air. Since the pioneering work by Raupp and Dibble [7,8], its photooxidation on TiO_2 has been widely studied on its kinetic and mechanistic aspects [9–13]. However, in order to allow the TiO_2 -based PCO to find application at large scale in the market, optimization of the remediation performances must be achieved. This optimization must include both the activity of the material used as photocatalyst and the geometry and characteristics of the reactor. Much effort has been dedicated in the past decade to the improvement of the TiO_2 photocatalytic activity for VOCs degradation [14–16]. Many attempts have focused on the preparation of TiO_2 using sol-gel based techniques [17–19]. The sol-gel approach allows control of the morphological and physicochemical properties of the synthesized materials by manipulation of the preparation conditions at a molecular level. The influence of the physicochemical properties of TiO_2 such as crystallinity, surface hydroxyl content and morphology (e.g., particle size, surface area, porous structure and particle agglomeration) on its photocatalytic activity has been extensively reported [20–23]. In particular, small particle size and high surface area have been related to high photocatalytic activity [18,20].

In this study, we report the photocatalytic performance of a range of titania photocatalysts obtained through a simple sol-gel approach followed by calcination. We discuss the effects of the physicochemical properties of TiO_2 on the degradation of TCE in air stream. The effect of the intensity of the incident radiation on photocatalytic activity was also investigated and compared with P-25 TiO_2 . In contrast with published work, we show that crystallinity over particle size and surface area is the crucial parameter which determines optimal photocatalytic activity.

2. Experimental

2.1. Sol-gel synthesis of TiO_2 particles

Titanium tetraisopropoxide (TTIP, Aldrich) as a titanium alkoxide precursor was added to isopropanol (*i*-PrOH, Fisher) under vigorous stirring at an *i*-PrOH/TTIP molar ratio of 30. When adding the TTIP solution into water dropwise, at a H_2O /TTIP molar ratio of 100, hydrolysis and condensation reactions occurred. After vigorous mixing of the slurry for 1 h, the TiO_2 particles were recovered with a fine filter paper (P2, Fisher), washed thoroughly with water, and dried at 50 °C for 2 h in an oven. The entrapped organic residues were extracted further with acetonitrile (Fisher) overnight. The as-synthesized amorphous TiO_2 particles were calcined in a multi-segment programmable furnace (Paragon Model HT-22-D, Thermcraft). The temperature was increased to 100 °C at a ramp rate of 3.0 °C/min to remove any traces of moisture and solvents and held for 1 h, and further increased up to 800 °C and held for 1 h. Commercial TiO_2 (P-25) was used as a reference photocatalyst to compare the activity of the catalysts prepared.

2.2. Materials characterization

The crystallographic properties of TiO_2 were investigated by X-ray diffraction (XRD) using a Kristalloflex D500 diffractometer (Siemens) with $\text{Cu K}\alpha$ ($\lambda = 1.5406 \text{ \AA}$) radiation. Crystal size of TiO_2 was calculated from Scherrer's equation based on broadening of the most intense diffraction peak for each polymorph. The diffraction angle 2θ was incremented from 20° to 60° with a step of 0.1 and time to step ratio of 1.0. The Brunauer, Emmett and Teller (BET) surface area, the Barrett, Joyner and Halenda (BJH) pore size distribution and pore the volume of TiO_2 particles were measured using N_2 adsorption/desorption isotherms on a porosimetry analyzer (Tristar 3000, Micromeritics). Before the measurement, the samples were purged with nitrogen gas for 2 h at 150 °C (or 12 h at 80 °C for those calcined at temperatures lower than 300 °C) using Flow prep 060 (Micromeritics). The morphology of TiO_2 particles was examined using a JEM-2010F (JEOL) high resolution transmission electron microscope (HR-TEM). The TiO_2 particles were dispersed in methanol using an ultrasonicator for 5 min and fixed on a carbon-coated copper grid (LC200-Cu, EMS) prior to the TEM analysis.

2.3. Film deposition

The TiO_2 catalysts were immobilized as thick film on borosilicate glass supports. Glass plates (75 mm × 100 mm) were cleaned by sonication in ethanol for 15 min, rinsed with ethanol and acetone and dried in air prior to coating. TiO_2 suspensions were prepared by dispersing a known amount of catalyst (0.45 g) by sonication in 10 ml of ethanol or methanol. The suspension was quickly deposited by pipetting on the glass support and the solvent was allowed to evaporate in air. Coated supports were dried in an oven at 80 °C overnight. Catalyst loading for all immobilized films was gravimetrically determined at approximately 6.0 mg/cm². Considering the density of TiO_2 , its loading and the surface area of the support, the film thickness was estimated to be approximately 1.5–2.0 μm .

2.4. Photocatalytic activity of catalyst specimens

The photocatalytic activity of the specimens was evaluated by measuring the rate of decomposition of trichloroethylene (TCE) (Fisher, purity >99.8%) in air in the presence of water vapour. A narrow slit, flat-plate, single-pass, flow-through photocatalytic reactor was used (Fig. 1) [24]. It consisted of a flat 75 mm-wide, 600 mm-long, stainless steel reactor that allowed the controlled distribution of the contaminated air flow over the catalyst. A 75 mm × 100 mm glass plate coated with the photocatalyst was located 270 mm from the inlet of the reactor and 170 mm from the outlet. The reactor was covered with a borosilicate glass (7.7 mm thick) sealed with a Viton gasket. This formed a 75 mm × 2.5 mm flow passage across the whole length of the reactor. The reactor inlet and outlet were designed to minimize back-flow dispersion and to achieve uniform, fully-developed flow before reaching the photocatalytic plate.

Synthetic air (BOC gases 80% N_2 , 20% O_2) was used as carrier gas. A humid stream was created by bubbling synthetic air in water while TCE vapors were fed into the dry stream through a washing bottle saturated with TCE vapors. Dry, humid and polluted streams were re-joined before the inlet of the reactor forming the gaseous mixture for the experiments. All flows were controlled by precision mass flow controllers (Cole-Parmer). The relative humidity (RH) was set by changing the flow rates of humid and dry streams, and constantly monitored by a thermohygrometer (Cole-Parmer) located before the reactor inlet. The reactor was irradiated with five black light blue fluorescent lamps (Philips TL 8W/08 F8T5/BLB,

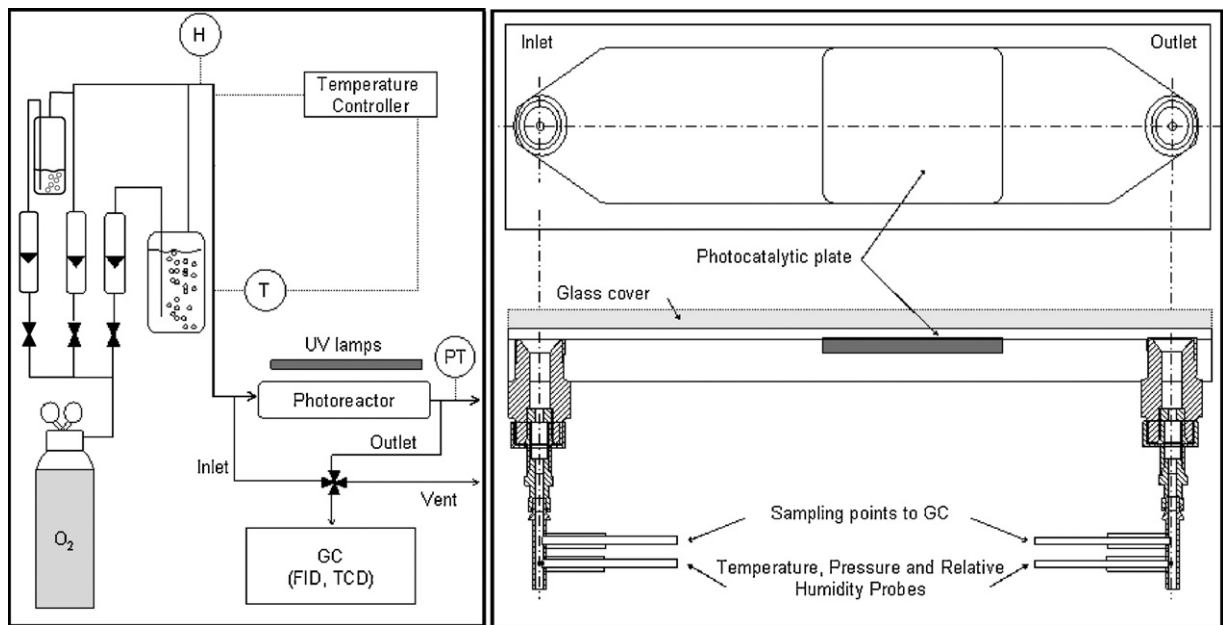


Fig. 1. Planar and side views of the flat-plate photocatalytic reactor and experimental set-up for the photocatalytic oxidation experiments.

0.0155 m bulb diameter, 0.26 m bulb length and 1.2 W UV-A output). The lamp emitted a minute fraction of the total radiation at 324 and 325 nm and the rest between 343 and 400 nm with a maximum irradiance peak at 365 nm. The centerlines of the lamps were separated by 0.039 m. The radiation intensity at the photocatalytic surface was regulated by changing the number of lamps switched on (1, 3 or 5). The distance of the lamps from the catalyst surface was 10 cm in order to ensure pseudo-uniform illumination of the entire surface of the coated support. An analysis of the radiation field on the surface of the photocatalyst has been reported previously [24].

UVA radiation was measured using a radiometer equipped with a 365 nm sensor (Cole-Parmer). The reactor inlet and outlet air streams were connected to a gas chromatograph (Agilent Technologies, GC-6890N) equipped with a GS-GASPRO capillary column for separation and a thermal conductivity detector (TCD) and a flame ionization detector (FID), through a system of automatic sampling valves. This system allows the analysis of the composition of the inlet and outlet samples and the calculation of TCE conversion during the experiment.

The experiments were conducted in the reaction controlled regime, using a total flow rate of 0.04 L/s, 8% relative humidity, and an initial concentration of TCE in synthetic air (20% O₂, 80% N₂, BOC gases) of 25 ± 3 μM (610 ± 42 ppmv). The incident photon flux on the supported catalyst was varied in the range 5.1–20.8 W/m². In a typical run, the TCE concentration and RH were allowed to stabilize, then the photocatalyst was irradiated, and the TCE conversion recorded once steady-state was re-established. TCE conversion was calculated from the difference between inlet and outlet air samples.

Experiments were carried out under “differential reactor” conditions (TCE conversions <10%), to permit estimation of the reaction rate from the conversion of TCE at steady-state as follow:

$$r_{\text{TCE}} = \frac{F \times [\text{TCE}]_0 \times X}{A} \quad (1)$$

where r_{TCE} is TCE reaction rate, F is the volumetric flow rate (L/s), $[\text{TCE}]_0$ is the initial TCE concentration (mol/L), X is TCE conversion at steady state and A is the surface of photocatalyst exposed to UV radiation (m²).

3. Results and discussion

3.1. Physicochemical properties.

The calcination procedure is critical to control the physicochemical properties of TiO₂ catalysts. As extensively investigated by Yu's group [25–27], the crystallographic (e.g., phase, crystallinity, size) and structural properties (e.g., surface area, pore volume) of TiO₂ particles greatly affect their photocatalytic activity. Consequently, it is important to understand these properties. The XRD patterns reported in Fig. 2 clearly revealed the amorphous nature of the as-synthesized TiO₂ and the TiO₂ calcined at low temperatures. At calcination temperature of 300 °C, the amorphous phase started transforming to the anatase phase with 5.8 nm crystal size. Increasing the temperature up to 600 °C, the anatase signal became stronger and the crystal size continued to increase to 27.8 nm. Further increase in the temperature led to the phase transformation of the anatase into rutile. TiO₂ calcined at 700 °C was a mixture of anatase and rutile (45:55) and that calcined at 800 °C was pure rutile.

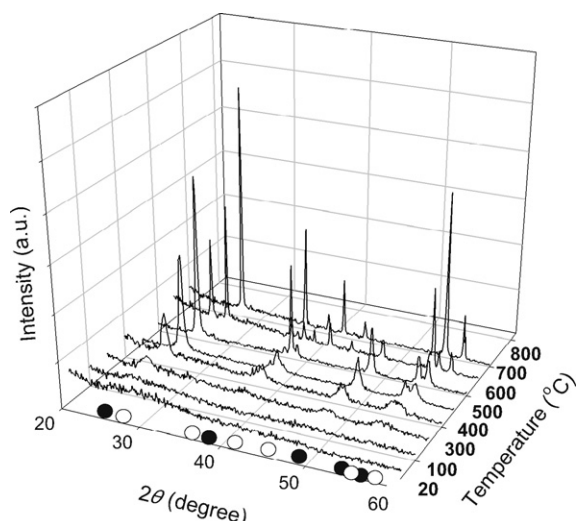


Fig. 2. Evolution of crystal phase upon calcination temperature. Solid and empty circles correspond to anatase and rutile crystal phases, respectively.

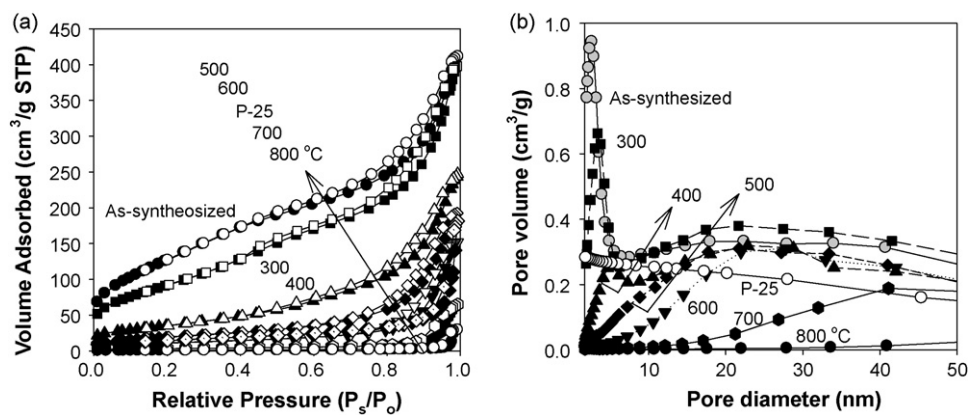


Fig. 3. Porosimetry analysis of TiO₂ particles: (a) N₂ adsorption and desorption isotherms and (b) pore size distribution.

Fig. 3 demonstrates the structural properties of TiO₂ particles, based on nitrogen adsorption/desorption isotherms. The as-synthesized TiO₂ particles exhibited a well-developed mesoporous structure. The pore size distribution indicates that the initial small pores below 4 nm are completely collapsed during thermal treatment. After calcination at 700 °C or above, no apparent mesoporous structure was seen. The structural properties of P-25 in terms of surface area, pore volume and crystal phase were very similar to those of TiO₂ prepared at 600–700 °C. However, the pore size distribution of P-25 was completely different from other TiO₂ particles. P-25 has well-defined 35 nm size nanoparticles. Its porous structure should be originated from the intra-particle space.

Table 1 summarizes the crystallographic and structural properties of TiO₂. The surface area and pore volume of calcined TiO₂ considerably decreased as the calcination temperature increased. The as-synthesized amorphous TiO₂ particles have high surface area (498 m²/g) and pore volume (0.65 cm³/g). Thermal treatment of the TiO₂ particles, caused the amorphous phase to compact and collapsed their porous structure. The crystal size increases with increasing calcination temperature and the surface area, pore volume and porosity decrease. The surface area and porosity of rutile TiO₂ were only 4.3 m²/g and 22.9%, respectively. The properties of P-25 (particle size: 30 ± 5 nm; surface area: 50 ± 5 m²/g; anatase content: 75%) were very similar to those of TiO₂ calcined at 600 °C.

Fig. 4 shows HR-TEM morphology of P-25 and TiO₂ catalysts prepared in this study. As indicated in each image, we also confirmed the crystal phase of some individual particles by directly reading d_{space} of lattices (shown in high magnification TEM image of the particles). P-25 (Fig. 4a) shows a mixture of anatase and rutile nanoparticles with well defined 30–40 nm size. Rutile in larger size rectangular shape was obviously differentiated from more or less spherical shaped smaller anatase. As

shown in Fig. 4b–f, changes in the morphology of TiO₂ catalysts over thermal treatment at up to 800 °C clearly show the effect of calcination on (i) the crystallization of amorphous TiO₂ to anatase (i.e., increase in crystallinity), (ii) particle growth, (iii) anatase transformation to rutile phase and (iv) collapse of porous structure. In general, the first two effects are beneficial and the last two effects are detrimental to high photocatalytic activity of TiO₂.

The as-synthesized amorphous TiO₂ (Fig. 4b) shows a well developed mesoporous structure, resulting in a high surface area and pore volume. Fig. 4c reporting TiO₂ calcined at 500 °C shows an agglomerated structure composed of 16 nm anatase nanoparticles. TiO₂ calcined at 600 °C (Fig. 4d) shows clear lattice fringes and well-developed grain boundary, indicating that the TiO₂ is highly crystalline. At temperatures higher than 600 °C, the anatase was transformed into rutile. TiO₂ calcined at 700 °C (Fig. 4e) shows well grown and crystallized TiO₂ but containing a mixture of 45% anatase and 55% rutile. Large size fully-grown 76 nm pure rutile nanoparticles were observed in TiO₂ obtained at 800 °C (Fig. 4f). The visible crystal size and phase are in good agreement with those determined from XRD. These crystallographic and structural properties of a series of TiO₂ samples and P-25 are closely associated with their photocatalytic activity to decompose TCE in air and the relation will be discussed in detail in the following sections.

3.2. Photocatalytic activity

TCE degradation was not detected in the dark or in absence of catalyst, therefore all variations in TCE concentration were ascribed to the photocatalytic activity of the catalyst. No reaction intermediates were detected by GC analysis under our experimental and analytical conditions. In the following discussion, TCE reaction rates are expressed per unit surface area of irradiated coated support.

Table 1
Structural and crystallographic properties of TiO₂.

Synthesis temperature (°C)	Structural				Crystallographic	
	S _{BET} ^a (m ² /g)	PV ^a (cm ³ /g)	Porosity (%)	PD ^a (nm)	Phase	CS ^a (nm)
As-synthesized	498	0.65	–	5.6	–	–
300	289	0.45	63.6	6.1	Anatase	5.8
400	132	0.37	59.0	10.1	Anatase	10.1
500	80.1	0.31	54.7	13.8	Anatase	15.8
600	42.7	0.23	47.2	20.7	Anatase	27.8
700	15.2	0.12	33.0	33.5	A45% + R55%	53.8
800	4.3	0.07	22.9	50.4	Rutile	75.8
P-25	55.4	0.28	52.4	20.6	A75% + R25%	35

^a S_{BET}: BET surface area, PV: pore volume, PD: BJH average pore diameter from N₂ adsorption isotherm, and CS: crystallite size measured from XRD.

^b A and R stand for anatase and rutile, respectively.

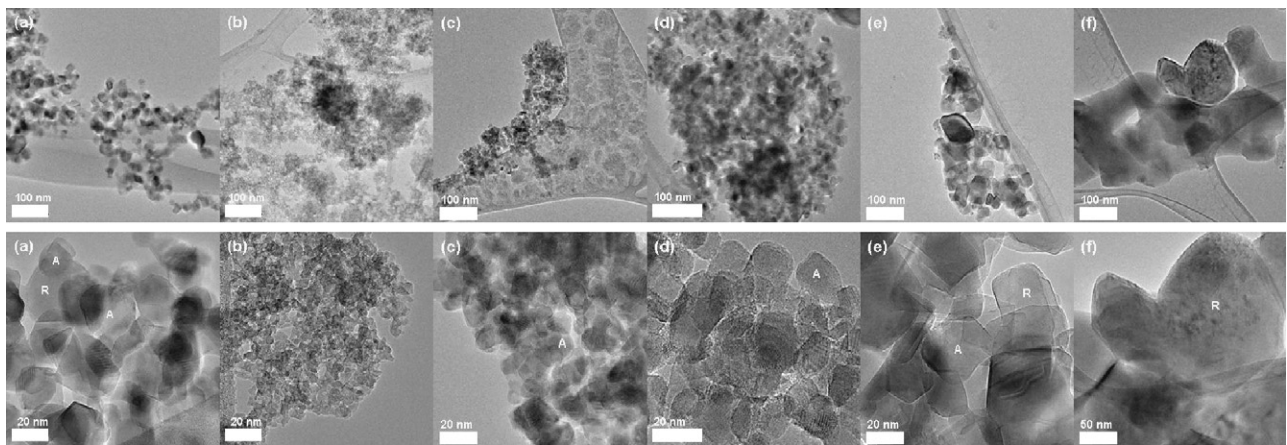


Fig. 4. HR-TEM morphology of TiO_2 particles: (a) P-25 (A75% + R25%), (b) as-synthesized TiO_2 (amorphous), (c) TiO_2 calcined at 500 °C, (d) TiO_2 calcined at 600 °C, (e) TiO_2 calcined at 700 °C (A45% + R55%), and (f) TiO_2 calcined at 800 °C. Note different scale bars at 20–100 nm. The crystal phase of some particles was indicated as A: anatase and R: rutile.

3.2.1. Effect of calcination temperature

Untreated TiO_2 did not show detectable TCE photoreduction, most probably because of the many defects sites originated from its amorphous nature, which capture electrons and holes generated. The conversion of TCE on TiO_2 samples calcined at different temperatures, in a humid air stream (RH = 8%) and under a UVA incident photon flux of 5.1 W/m² is reported in Fig. 5. The conversion increases progressively with calcination temperature in the range 300–600 °C. The highest performance was obtained with TiO_2 treated at 600 °C, conversely, heat treatment at higher temperatures led to a drastic drop of activity. The above results clearly illustrate that the degree of crystallinity is more important than surface area and/or crystal size in determining the level of activity of anatase TiO_2 samples prepared by sol–gel followed by thermal treatment. TiO_2 with high crystallinity is characterized by longer charge carrier lifetime thus associated with more efficient electron–hole utilization. High degree and quality of crystallization means the presence of fewer TiO_2 bulk defects, where photoexcited electron and holes can recombine. Yu et al. recently observed the same activity trend for acetone mineralization in gas phase, using hydrothermally prepared TiO_2 in the size range of 5.3–7.1 nm [28].

Meanwhile the porosity and surface area of TiO_2 particles affect the transport and adsorption capacity of reactants on the catalyst active sites [29–31]. In addition, Maira et al. [18] have reported crystal size to be an important property that determines the activity of TiO_2 specimens. The degradation rates of TCE on pure

anatase obtained by sol–gel followed by hydrothermal treatment, exhibited a maximum when the TiO_2 crystal size was 7 nm (surface area 150 m²/g). A reduction in activity was observed in TiO_2 samples with crystal size larger than 7 nm, which was ascribed to the smaller surface area of the specimens. Conversely, a quantum size effect, which leads to a blue shift in the TiO_2 absorption and consequent lower utilization of photons at the catalyst surface was called upon to explain lower activity observed in samples with 2.3 and 5.2 nm.

The phase composition also has a crucial impact on the photocatalytic activity. It is well known that anatase phase shows considerably higher photoactivity than rutile. Samples calcined up to 600 °C are made up of pure anatase. In samples prepared at 700 and 800 °C, the further growth of the crystals is accompanied by phase transformation: samples calcined at 700 and 800 °C contain 55% and 100% rutile, respectively. Many studies have pointed out a linear relationship between crystal size and the photocatalytic activity for TCE photo-oxidation in liquid phase as long as no significant rutile phase is present in the samples [32,33]. Our results for the decomposition of TCE in gas phase clearly report a similar trend, and confirm that the use of high calcination temperatures without formation of rutile is important to achieve highly active photocatalysts. We believe that the increase in the crystallinity of anatase TiO_2 upon calcination overcame the depreciation in its structural properties (lower surface area and porosity) and appears to be the determinant factor for the improved decomposition rates of TCE observed.

3.2.2. Effect of intensity of incident radiation and comparison with P-25

The effect of the intensity of the incident UVA radiation on the photocatalytic performance of the TiO_2 specimens was studied in the range 5.1–20.8 W/m². TCE degradation in the gas phase has been investigated by Keshmiri et al. using similar reactor geometry and experimental conditions [34,35]. They used TiO_2 composites prepared by binding P-25 with titania sol. The performances of such coatings were comparable, but did not exceed those of untreated P-25. Fig. 6 shows the TCE rate constant for TiO_2 and P-25 under different radiation intensities. TiO_2 specimens calcined at 400–600 °C exhibited consistently higher photoactivity than P-25 in the range of intensities studied. The TiO_2 specimens calcined at 300, 700 and 800 °C showed lower activity than P-25. P-25 is considered one of the most active photocatalyst, and its activity is believed to arise from its phase composition (75% anatase, 25% rutile) and from the good particle contact between anatase and rutile. In P-25, rutile acts as charge carrier separator, increasing the

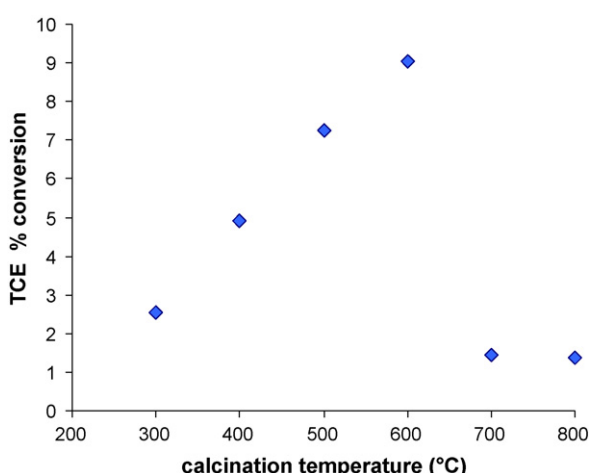


Fig. 5. TCE conversion % as function of calcinations temperature (light $I = 5.12 \text{ W/m}^2$).

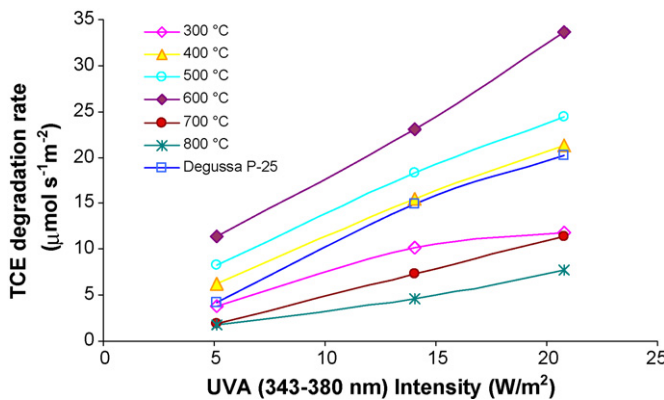


Fig. 6. TCE degradation rate as function of incident light intensity.

lifetime of electron–hole pair. All pure anatase TiO_2 here showed improved activity compared with P-25. On the contrary, pure rutile phase obtained by calcination at 800 °C showed negligible activity. The charge carrier separation mechanism responsible for P-25 properties is not effective in the sample calcined at 700 °C and composed of 45% rutile and 55% anatase.

It is worth to note that the difference in performance among the catalysts is more apparent at low radiation intensity. The reaction rate constant for the most active catalyst (600 °C) is approximately 3 times higher than that of P-25 under low irradiation intensity (5.1 W/m²) while it is only 1.5 times higher at a higher irradiation intensity (20.8 W/m²). Therefore, under conditions of low UVA illumination such as those found in living indoor environments which are in the order of mW/m², the most active catalyst specimen (600 °C) should outperform commercial P-25.

The relation between the intensity of incident radiation I and the observed photocatalytic reaction rate r has been shown both theoretically and experimentally to follow power law ($r \propto I^m$) with $0.5 < m < 1.0$. The value of m is related to the efficiency of electron–hole formation, trapping and recombination at the

catalyst surface. It is usually observed that in the low intensity region, the reaction rate increases linearly with light intensity ($m = 1$); while in the high intensity region it increases with the square root of intensity ($m = 0.5$). When the correlation is linear, the photon harvesting is efficient and electron–hole pair formed are consumed by the chemical process, while under half-order conditions ($m = 0.5$), the recombination of electron–hole pairs is considered to be the dominant process on the catalyst surface.

Considering a 21 steps elementary reaction mechanism of TCE (Table 2), we have recently shown that the rate of photocatalytic oxidation of TCE over TiO_2 films can be represented by the following expression [36,37] when $K_{\text{TCE}}[\text{TCE}] \ll 1 + K_{\text{W}}[\text{H}_2\text{O}]$:

$$-r_{\text{TCE}} = \frac{\alpha_1[\text{TCE}][\text{H}_2\text{O}]}{(1 + K_{\text{W}}[\text{H}_2\text{O}])(1 + K_{\text{W}}[\text{H}_2\text{O}] + \alpha_3[\text{TCE}])} \times \left(\sqrt{1 + \alpha_2 \langle \varphi \rangle \langle I \rangle \frac{(1 + K_{\text{W}}[\text{H}_2\text{O}])}{[\text{H}_2\text{O}]}} - 1 \right) \quad (2)$$

where α_1 , α_2 and α_3 are kinetic constants:

$$\alpha_1 = \frac{k_1 k_2 k_7 K_{\text{TCE}} K_{\text{W}} [\text{O}_2][\text{S}]}{2 k_{17} k_{18} [\text{M}]} \quad (3)$$

$$\alpha_2 = \frac{4k_{17}}{k_1 k_2 k_{\text{W}} [\text{O}_2][\text{S}]} \quad (4)$$

$$\alpha_3 = \frac{\alpha_1 K_{\text{TCE}} [\text{S}]}{k_{18} [\text{M}]} \quad (5)$$

K_{W} is the water adsorption/desorption constant onto TiO_2 , $\langle \varphi \rangle$ is the wavelength averaged quantum efficiency (i.e., the number of electron–hole couples generated per incident photon) and $\langle I \rangle$ is the wavelength averaged incident photon flux, which in general is a function of position over the titania-coated glass-plate. Eq. (2) can be simplified to the limiting conditions of high and low photon flux. At high photon flux the 1 in the term in parenthesis can be neglected and the rate shows half-order dependence on $\langle I \rangle$. This limiting case has been described by Upadhyay and Ollis [38]. At low

Table 2
TCE reaction mechanism.

Process	Reaction	Reaction rate	Nr
Initiation	$\text{TiO}_2 \xrightarrow{h\nu} \text{TiO}_2 + e^- + h^+$ $h^+ + \text{H}_2\text{O}_{\text{ad}} \rightarrow \text{OH}^\cdot + \text{H}^+$ } $h^+ + \text{HO}_{\text{ad}} \rightarrow \text{OH}^\cdot$ $e + \text{O}_2 \rightarrow \text{O}_2^\cdot$	r_g $k_1[\text{H}_2\text{O}]_{\text{ad}}[h^+]$ $k_2[\text{O}_2][e^-]$	(R0) (R1) (R2)
Cl^\cdot generation	$\text{HC}_2\text{Cl}_3 + \text{OH}^\cdot \rightarrow \text{HC}_2\text{Cl}_3\text{OH}^\cdot$ $\text{HC}_2\text{Cl}_3\text{OH}^\cdot + \text{O}_2 \rightarrow \text{HC}_2\text{Cl}_3\text{OHOO}^\cdot$ $\text{HC}_2\text{Cl}_3\text{OHOO}^\cdot \rightarrow \text{HC}_2\text{Cl}_3\text{OHO}^\cdot + \frac{1}{2}\text{O}_2$ $\text{HC}_2\text{Cl}_3\text{OHO}^\cdot \rightarrow \text{HC}_2\text{Cl}_2\text{HO} + \text{Cl}^\cdot$	$k_3[\text{TCE}]_{\text{ad}}[\text{OH}^\cdot]$ $k_4[\text{HC}_2\text{Cl}_3\text{OH}^\cdot][\text{O}_2]$ $k_5[\text{HC}_2\text{Cl}_3\text{OHO}^\cdot]$ $k_6[\text{HC}_2\text{Cl}_3\text{OHO}^\cdot]$	(R3) (R4) (R5) (R6)
Chain propagation	$\text{HC}_2\text{Cl}_3^\cdot + \text{Cl}^\cdot \rightarrow \text{HC}_2\text{Cl}_4^\cdot$ $\text{HC}_2\text{Cl}_4^\cdot + \text{O}_2 \rightarrow \text{HC}_2\text{Cl}_4\text{OO}^\cdot$ $\text{HC}_2\text{Cl}_4\text{OO}^\cdot \rightarrow \text{HC}_2\text{Cl}_4\text{O}^\cdot + \frac{1}{2}\text{O}_2$ $\text{HC}_2\text{Cl}_4\text{O}^\cdot \rightarrow \text{COCl}_2 + \text{HCl}_2^\cdot$ $\text{HC}_2\text{Cl}_4\text{O}^\cdot \rightarrow \text{HC}_2\text{OCl}_3 + \text{Cl}^\cdot$	$k_7[\text{TCE}]_{\text{ad}}[\text{Cl}^\cdot]$ $k_8[\text{HC}_2\text{Cl}_4^\cdot]_{\text{ad}}[\text{O}_2]$ $k_9[\text{HC}_2\text{Cl}_4\text{O}^\cdot]$ $k_{10}[\text{HC}_2\text{Cl}_4\text{O}^\cdot](10\%)$ $k_{11}[\text{HC}_2\text{Cl}_4\text{O}^\cdot](90\%)$	(R7) (R8) (R9) (R10) (R11)
Phosgene formation and DCAC consumption	$\text{HC}_2\text{OCl}_3 + \text{OH}^\cdot \rightarrow \text{C}_2\text{Cl}_3\text{O}^\cdot + \text{H}_2\text{O}$ $\text{C}_2\text{Cl}_3\text{O}^\cdot + \text{O}_2 \rightarrow \text{OOC}_2\text{Cl}_3\text{O}^\cdot$ $\text{OOC}_2\text{Cl}_3\text{O}^\cdot \rightarrow \text{OC}_2\text{Cl}_3\text{O}^\cdot + \frac{1}{2}\text{O}_2$ $\text{OC}_2\text{Cl}_3\text{O}^\cdot \rightarrow \text{CCl}_2\text{O} + \text{CClO}^\cdot$ $\text{CClO}^\cdot \rightarrow \text{CO} + \text{Cl}^\cdot$	$k_{12}[\text{DCAC}][\text{OH}^\cdot]$ $k_{13}[\text{C}_2\text{Cl}_3\text{O}^\cdot][\text{O}_2]$ $k_{14}[\text{OOC}_2\text{Cl}_3\text{O}^\cdot]$ $k_{15}[\text{OC}_2\text{Cl}_3\text{O}^\cdot]$ $k_{16}[\text{CClO}^\cdot]$	(R12) (R13) (R14) (R15) (R16)
Ending reactions	$e^- + h^+ \rightarrow \text{heat}$ $\text{Cl}^\cdot + \text{M} \rightarrow \text{products}$	$k_{17}[\text{h}^+][e^-]$ $k_{18}[\text{Cl}^\cdot][\text{M}]$	(R17) (R18)
Non-radical reaction	$\text{COCl}_2 + \text{H}_2\text{O} \rightarrow \text{CO}_2 + 2\text{HCl}$		(R19)
TCE adsorption/desorption	$\text{HC}_2\text{Cl}_3 + \text{S} \leftrightarrow \text{HC}_2\text{Cl}_3$	$k_A(K_{\text{TCE}}[\text{TCE}][\text{S}] - [\text{TCE}]_{\text{ad}})$	(R20)
Water adsorption/desorption	$\text{H}_2\text{O} + \text{S} \leftrightarrow \text{H}_2\text{O}_{\text{ad}}$	$k_{\text{W}}(K_{\text{W}}[\text{H}_2\text{O}][\text{S}] - [\text{H}_2\text{O}]_{\text{ad}})$	(R21)

Notes: Trichloroethylene: HC_2Cl_3 ; dichloroacetyl chloride: HC_2OCl_3 ; phosgene: COCl_2 .

Table 3
Values of m and correlation coefficients.

Synthesis temperature (°C)	m	R^2
300	0.85 ± 0.13	0.977
400	0.89 ± 0.20	0.999
500	0.77 ± 0.01	0.999
600	0.75 ± 0.04	0.993
700	1.26 ± 0.04	0.999
800	1.06 ± 0.08	0.995
Degussa P-25	1.15 ± 0.07	0.991

photon flux the term under the square root can be expanded in Taylor's series truncated to the first term to give:

$$-r_{\text{TCE}} = \langle I \rangle \frac{\alpha[\text{TCE}]}{(1 + K_W[\text{H}_2\text{O}] + \alpha_3[\text{TCE}])} \quad \text{with } \alpha = \frac{\alpha_1 \alpha_2 \langle \varphi \rangle}{2} \quad (6)$$

Values of reaction rate as function of the intensity of the incident radiation were used to plot $\log r$ vs. $\log I$ to estimate the value of m for all samples under study. Table 3 summarizes the values of m of the TiO_2 specimens used in this study. Previous studies reported that TCE degradation on commercial P-25 follows a pseudo first-order regime for photon fluxes up to 28.1 W/cm^2 [12,24,39] and this trend was confirmed in our experiments which show a value of m equal to 1.15 (note that this is slightly higher than 1 possibly, due experimental error). Pseudo first order-dependence was also found for the samples calcined at 700 and 800 °C. Conversely, the values of the coefficient m for the TiO_2 anatase samples calcined from 300 to 600 °C were found to vary from 0.75 to 0.89. If we assume that the binding constant of water K_W on titania, does not vary over the samples investigated, the above findings imply that the product $(\alpha_2 \langle \varphi \rangle)$ in Eq. (2) is higher in the pure anatase samples than in the samples with rutile. This suggest that the pure anatase titania samples may have one or all of the following: (1) a higher quantum efficiency compared to rutile; (2) a higher rate of electron–hole recombination compared to rutile; (3) a lower rate of electron–hole trapping.

3.3. Importance of crystallographic and morphological properties of TiO_2 and implications of the role of rutile

The mechanisms of the relative reactivity of anatase, rutile and their mixture are still poorly understood. In general, anatase particles are much more active than rutile in the photocatalytic oxidation of organic compounds in water and air. This effect has often been attributed to the larger surface area of anatase compared to rutile, the higher affinity of anatase for organic compounds, and larger band gap (3.2 vs. 3.0 eV for rutile). Furthermore, it has been observed that the reduction of molecular oxygen at the surface of anatase, yields mainly hydrogen peroxide and partially superoxide anion radical, while at the surface of rutile it yields superoxide anion radical only [40]. This difference may also add to the higher photocatalytic activity of anatase over rutile. The activity and role of rutile is still controversial. In general, its reactivity is very poor. However, a study demonstrated that when similar crystallite sizes and surface areas of rutile and anatase were prepared, rutile was more active than anatase [41]. Another study concluded that the rutile phase is active or inactive, depending on its preparation conditions [42].

The mixture of TiO_2 rutile/ TiO_2 anatase has shown that synergistic effects may take place at appropriate mole ratios. The established high reactivity of the mixed phase TiO_2 such as P-25 (25% rutile, 75% anatase) could be attributed to the synergy of the anatase and rutile particles leading to spatial charge separation and hindered recombination [43]. Under appropriate conditions it

has been observed that the photogenerated charge carriers available for the surface reaction increase [44]. The detail mechanism of facilitated charge separation and transfer is still under debate. General speculation suggests that charge separation occurs on the anatase phase and rutile acts as an electron sink. However, Hurum et al. [45] proposed a new explanation which calls for the rapid electron transfer from rutile to lower energy anatase lattice trapping sites, leading to a more stable charge separation. The transfer of the photogenerated electron to anatase lattice trapping sites allows holes that would have been lost to recombination to reach the surface. Subsequent electron-transfer moves the electron from anatase trapping sites to surface trapping sites, further separating the electron–hole pair. Regardless of the theories that have been proposed, the lower electron–hole recombination rate in either case is a plus for the mixed phase TiO_2 in addition to the general advantages of anatase TiO_2 .

Yan et al. [46] conducted an interesting experiment on the effect of rutile content in TiO_2 but with relatively similar surface area and crystallinity. Their results showed that an increase in the rutile content, up to 30%, slightly enhanced the decomposition of methyl orange but its further increase rather reduced the reactivity of TiO_2 . This can be interpreted with two counter-intuitive effects: the presence of rutile is beneficial to the spatial charge separation but in large amount of rutile the inherent advantages of anatase are being lost leading to decrease in photoactivity. This supports the presence of an optimum amount of rutile phase in TiO_2 .

In addition to the amount of rutile, its physical contact configuration to anatase is another important issue. A study found that small rutile crystallites properly surrounded by anatase particles form highly active clusters where rutile absorbs a wide range of radiant energy, leading to charge separation that is stabilized by electron transfer to lower energy surface traps on anatase [45]. Many research studies pointed out that the synergistic effect really depends on the morphology of anatase–rutile interfaces [45,47,48].

The highest reactivity of anatase TiO_2 calcined at 600 °C and extremely low reactivity of pure rutile TiO_2 obtained at 800 °C, reported in this work, are easily understandable. The low catalytic activity of TiO_2 calcined at 700 °C, in spite of its anatase–rutile mixture characteristic, might be ascribed to too high rutile content (55%) as well as poor configuration of anatase/rutile connection for charge separation and transfer. Moreover the sample calcined at 700 °C shows a low surface area which certainly contributes to decrease in photocatalytic activity. Although the reactivity of anatase, rutile, and their mixture is complex, in general, fully grown anatase with high crystallinity is the most active, anatase properly connected with an optimum amount of rutile might show enhanced reactivity, and rutile is much less active. In case of the same crystallographic properties, TiO_2 particles with higher surface area are more reactive.

P-25 is a mixture of rutile and anatase likewise our TiO_2 specimen calcined at 700 °C while the sample calcined at 800 °C is made of pure rutile. These results strongly suggest that the presence of a rutile phase in the catalyst favors electron–hole utilization for redox reactions and minimize electron–hole recombination. We may also argue that the more compact structure of the rutile phase compared to anatase allows for a smaller concentration of defects sites and faster transfer of charges to the surface and therefore a lower percentage of electron–hole recombination. However, the lower surface area and porosity exhibited by these samples is called upon to justify the lower rate of TCE oxidation observed. The main advantage of P-25 compared to our sample containing rutile is the much larger surface area and porosity. The rate of photocatalytic oxidation of TCE over P-25 and rutile-containing TiO_2 specimens can therefore be represented by Eq. (6), under the above range of photon fluxes, with the

parameters α , α_3 and K_W which are dependant on the physico-chemical properties of the catalyst prepared.

The TiO_2 samples containing pure anatase exhibited m values between 0.5 and 1 suggesting that a higher degree of electron–hole recombination occurs in these specimens compared to the sample containing a rutile phase. As a result the dependence of the rate on light intensity becomes complex. In this case the full rate equation shown in Eq. (2) should be used to model the rate of photocatalytic oxidation of TCE. The higher rates of oxidation exhibited by the samples calcined at temperatures between 400 and 600 °C should be attributed to the presence of a mesoporous structure as previously described in Fig. 3 [30,31], to a progressively lower concentration of defects in the anatase structure at higher calcination temperatures and to an increase in the rate of electron–hole couple generated per incident photon (quantum efficiency) represented by the parameter $\langle\varphi\rangle$ in Eq. (2).

4. Conclusions

The calcination procedure greatly affected the physicochemical properties of TiO_2 . The results presented show that crystallinity, rather than surface area or porosity, is the crucial parameter that favors the photocatalytic oxidation of TCE over TiO_2 made of pure anatase. Pure anatase titania obtained by treatment at temperature between 400 and 600 °C exhibited much higher photocatalytic activity than commercial P-25. The enhanced activity should be attributed to the presence of a mesoporous structure, to a progressively lower concentration of defects in the anatase structure at higher calcination temperatures and to an increase in the rate of electron–hole couple generated per incident photon (quantum efficiency). The presence of rutile at a high content (55%) was found to have adverse effects on the photoactivity of TiO_2 , other than in P-25. However, rutile appears to be a better catalyst than anatase at utilizing “absorbed” photons for redox reactions ($m = 1$ for rutile; $0.5 < m < 1$ for samples containing pure anatase) although lower activity of pure rutile is the results of lower porosity, lower surface area and possibly a higher photon scattering albedo compared to anatase [49], since photons have less chance to enter the pore structure of the catalyst (i.e., lower quantum efficiency compared to anatase).

Acknowledgements

Gianluca Li Puma gratefully acknowledges the financial support of the University of Nottingham (Knowledge Transfer Innovation Award, KT052) and NATO (grant CBP.EAP.SFPP 982835). Dionysios D. Dionysiou and Hyeok Choi acknowledge funding for their contribution from the US National Science Foundation through a CAREER Award (BES-0448117) to Dionysios D. Dionysiou.

References

- [1] S.T.M. Michael, R. Hoffmann, W. Choi, D.W. Banham, Chem. Rev. 95 (1995) 69.
- [2] J. Zhao, X. Yang, Build. Environ. 38 (2003) 645.
- [3] D.S. Bhatkande, V.G. Pangarkar, A.A.C.M. Beenackers, J. Chem. Technol. Biotechnol. 77 (2001) 102.
- [4] D.F. Ollis, C. R. Acad. Sci. Paris, Série Iic, Chimie/Chem. 3 (2000) 405.
- [5] A.L. Linsebigler, G. Lu, J.T. Yates, Chem. Rev. 95 (1995) 735.
- [6] W. Choi, J. Ryo, SP-2 Second International Conference on ‘Semiconductor Photochemistry’, Aberdeen, 23rd–25th July, 2007.
- [7] L.A. Dibble, G.B. Raupp, Catal. Lett. 4 (1990) 345.
- [8] L.A. Dibble, G.B. Raupp, Environ. Sci. Technol. 26 (1992) 492.
- [9] W.A. Jacoby, M.R. Nimlos, D.M. Blake, R.D. Noble, C.A. Koval, Environ. Sci. Technol. 28 (1994) 1661.
- [10] W.A.J.M.R. Nimlos, D.M. Blake, T.A. Millne, Environ. Sci. Technol. 27 (1993) 732.
- [11] K.-H. Wang, J.-M. Jehng, Y.-H. Hsieh, C.-Y. Chang, J. Hazard. Mater. 90 (2002) 63.
- [12] S.B. Kim, S.C. Hong, Appl. Catal. B: Environ. 35 (2002) 305.
- [13] S. Yamazaki-Nishida, K.J. Nagano, L.A. Phillips, S. Cervera-March, M.A. Anderson, J. Photochem. Photobiol. A: Chem. 70 (1993) 95.
- [14] M.C. Hidalgo, D. Bahmann, Appl. Catal. B: Environ. 61 (2005) 259.
- [15] A. Huang, L. Cao, J. Chen, F.-J. Spiess, S.L. Suib, T.N. Obee, S.O. Hay, J.D. Freihaut, J. Catal. 188 (1999) 40.
- [16] G.-M. Zuo, Z.-X. Cheng, H. Chen, G.-W. Li, T. Miao, J. Hazard. Mater. 128 (2006) 158.
- [17] X. Fu, W.A. Zeltner, M.A. Anderson, Appl. Catal. B: Environ. 6 (1995) 209.
- [18] A.J. Maira, K.L. Yeung, C.Y. Lee, P.L. Yue, C.K. Chan, J. Catal. 192 (2000) 185.
- [19] M.A. Anderson, M.J. Gieselmann, Q. Xu, J. Membr. Sci. 39 (1988) 243.
- [20] A.J. Maira, K.L. Yeung, J. Soria, J.M. Coronado, C. Belver, C.Y. Lee, V. Augugliaro, Appl. Catal. B: Environ. 29 (2001) 327.
- [21] K.L. Yeung, S.T. Yau, A.J. Maira, J.M. Coronado, J. Soria, P.L. Yue, J. Catal. 219 (2003) 107.
- [22] Y. Chen, E. Stathatos, D.D. Dionysiou, Surf. Coat. Technol. 202 (2008) 1944.
- [23] D.S. Kim, S.J. Han, S.-Y. Kwak, J. Colloid Interface Sci. 316 (2007) 85.
- [24] I. Salvado-Estivill, D.M. Hargreaves, G. Li Puma, Environ. Sci. Technol. 41 (2007) 2028.
- [25] J. Yu, W. Wang, B. Cheng, B. Su, J. Phys. Chem. C 113 (2009) 6743.
- [26] J. Yu, Y. Su, B. Cheng, Adv. Funct. Mater. 17 (2007) 1984.
- [27] J. Yu, H. Yu, B. Cheng, X. Zhao, J. Yu, W. Ho, J. Phys. Chem. B 107 (2003) 13871.
- [28] J. Yu, G. Wang, B. Cheng, M. Zhou, Appl. Catal. B: Environ. 69 (2007) 171.
- [29] Y.V. Kolen'ko, B.R. Churagulov, M. Kunst, L. Mazerolles, C. Colbeau-Justin, Appl. Catal. B: Environ. 54 (2004) 51.
- [30] J. Yu, S. Liu, H. Yu, J. Catal. 249 (2007) 59.
- [31] J. Yu, L. Zhang, B. Cheng, Y. Su, J. Phys. Chem. C 111 (2007) 10582.
- [32] K.Y. Jung, S.B. Park, J. Photochem. Photobiol. A: Chem. 127 (1999) 117.
- [33] K.Y. Jung, S.B. Park, S.-K. Ihm, Appl. Catal. A: Gen. 224 (2002) 229.
- [34] M. Keshmiri, M. Mohseni, T. Troczynski, Appl. Catal. B: Environ. 53 (2004) 209.
- [35] M. Keshmiri, T. Troczynski, M. Mohseni, J. Hazard. Mater. 128 (2006) 130.
- [36] I. Salvado-Estivill, PhD Thesis University of Nottingham, 2007.
- [37] G. Li Puma, I. Salvado-Estivill, T.N. Obee, S.O. Hay, Sep. Purif. Technol. 67 (2009) 226.
- [38] S. Upadhyay, D.F. Ollis, J. Adv. Oxid. Technol. 3 (1998) 199.
- [39] W.A. Jacoby, D.M. Blake, R.D. Noble, C.A. Koval, J. Catal. 157 (1995) 87.
- [40] H. Goto, Y. Hanada, T. Ohno, M. Matsumura, J. Catal. 225 (2004) 223.
- [41] Q. Zhang, L. Gao, J. Guo, Appl. Catal. B: Environ. 26 (2000) 207.
- [42] A. Sclafani, L. Palmisano, M. Schiavello, J. Phys. Chem. 94 (1990) 829.
- [43] T. Miyagi, M. Kamei, T. Mitsuhashi, T. Ishigaki, A. Yamazaki, Chem. Phys. Lett. 390 (2004) 399.
- [44] T. Kawahara, Y. Konishi, H. Tada, N. Tohge, J. Nishii, S. Ito, Angew. Chem. Int. Ed. 41 (2002) 2811.
- [45] D.C. Hurum, A.G. Agrios, K.A. Gray, T. Rajh, M.C. Thurnauer, J. Phys. Chem. 107 (2003) 4545.
- [46] M. Yan, F. Chen, J. Zhang, M. Anpo, J. Phys. Chem. 109 (2005) 8673.
- [47] D.C. Hurum, K.A. Gray, T. Rajh, M.C. Thurnauer, J. Phys. Chem. 109 (2005) 977.
- [48] T. Ohno, K. Sarukawa, K. Tokieda, M. Matsumura, J. Catal. 203 (2001) 82.
- [49] D. Reyes-Coronado, G. Rodríguez-Gattorno, M.E. Espinosa-Pesqueira, C. Cab, R. de Coss, G. Oskam, Nanotechnol 19 (2008) 145605.